Available online at www.sciencedirect.com

SciVerse ScienceDirect

Acta Materialia 60 (2012) 1610–1622

Acta MATERIALIA

www.elsevier.com/locate/actamat

Length scale-dependent deformation behavior of nanolayered Cu/Zr micropillars

J.Y. Zhang [a,b], S. Lei [a], Y. Liu [b], J.J. Niu [a], Y. Chen [b], G. Liu [a,*], X. Zhang [b,*], J. Sun [a,*]

[a] State Key Laboratory for Mechanical Behavior of Materials, Xi'an Jiaotong University, Xi'an 710049, People's Republic of China
[b] Department of Mechanical Engineering, Materials Science and Engineering Program, Texas A&M University, College Station, TX 77843-3123, USA

Received 12 August 2011; received in revised form 30 October 2011; accepted 1 December 2011
Available online 1 February 2012

Abstract

The mechanical behavior of incoherent Cu/Zr multilayers was studied in uniaxial compression experiments using micropillars with individual layer thicknesses (h) ranging from 5 to 100 nm. The deformation behavior of these micropillars are size dependent, transiting from dislocation dominated symmetrical slip at large h to shear localization induced by asymmetric slip and grain boundary mediated deformation at small h. During compression studies the multilayer micropillars exhibit a transition from strain hardening to shear softening at small h, and work softening at greater h. A maximum strain hardening rate is observed at a critical h of 20 nm, which was explained in terms of a transition from dislocation interactions to cross-slip of dislocations. The mechanical strength of the micropillars is also dependent on h, which was quantitatively analyzed using the confined layer slip model. In addition, the influence of pillar diameter on the mechanical behavior is also investigated. The effect of extrinsic size on the deformation mechanisms is discussed with respect to the intrinsic size effect with variation in h.

Keywords: Nanolayered micropillar; Plastic deformation; Strain hardening; Strain softening; Strength

1. Introduction

Nanostructured metallic multilayers are ideal systems for the exploration of length scale-dependent plasticity. Certain multilayers have extraordinary strength and ductility when the individual layer thickness (h) is of the order of a few nanometers [1–6]. For instance, when h is ~2–10 nm the strength (estimated as 1/3 of the nanoindentation hardness) of the multilayer may be as high as 1/2 to 1/3 of the theoretical strength [7–9]. On the nanoscale the interfaces between the two constituents of the multilayer play an increasingly important role in determining the mechanical properties as they comprise a significant volume fraction of the multilayer when h decreases to 10 nm or less [8–12].

In traditional nanoindentation hardness measurements with a sharp indenter tip the plastic zone shows a non-uniform stress state within the sample, thereby making interpretation of the plastic flow behavior complicated and not permitting observation of the strain hardening/softening behavior [5,13]. The development of a micropillar compression technique has opened up new routes for studying the mechanical properties of materials at small length scales in a nominally homogeneous stress state [13–16], and has been successfully used to investigate the mechanical response of single crystal metals [17–21], nanocrystalline materials [22–24], metallic alloys [25,26] and multilayer composites [1–3,27,28]. Several important phenomena have emerged from single crystalline pillar compression experiments: (i) the size-dependent yield strength, which is commonly explained by the source truncation [29] or the source starvation/exhaustion mechanism [30–32]; (ii) intermittent flow [33], caused by dislocation avalanches [34].

* Corresponding authors. Tel.: +86 29 82667143; fax: +86 29 82663453 (J. Sun).
E-mail addresses: lgsammer@mail.xjtu.edu.cn (G. Liu), zhangx@tamu.edu (X. Zhang), junsun@mail.xjtu.edu.cn (J. Sun).

1359-6454/$36.00 © 2011 Acta Materialia Inc. Published by Elsevier Ltd. All rights reserved.
doi:10.1016/j.actamat.2011.12.001

In bulk coarse-grained fcc metals dislocation motion in the form of pile-ups on multiple slip systems results in the formation of Lomer–Cottrell type barriers created by intersection of dislocations from different slip systems. With increasing strain dislocation tangles develop and eventually result in a cell structure with a high dislocation density within the cell walls and low density within cells. This refers to the well-established macroscopic strain hardening concept of (fcc) metals, which is governed by strain-driven dislocation storage [35]. The maximum work hardening rate in this mechanism (stage II) in single crystals is of the order of $\mu/200$, where μ is the shear modulus (roughly equivalent to $E/50$ in polycrystals, with E being the Young's modulus) [35]. With a further increase in strain the work hardening rate drops (stage III) due to cross-slip and a corresponding significant rearrangement/dynamic recovery of dislocations. In nanocrystalline fcc metals dislocations may be emitted from and absorbed by grain boundaries (GB) with little accumulation within grains [36–39], providing support to the general belief that they have a low strain hardening rate.

In contrast, during compression testing of Al/Al_3Sc micropillars [5] (diameter $\sim$ 300 nm) the deformation behavior evolved from strain softening to strain hardening as the layer thickness increased, as was also demonstrated in Cu/Nb micropillars [1,2], due to a transition of the deformation mechanism from dislocations cutting across the interface to single dislocation movement in the confined layers [40,41]. Recently Misra et al. [42] investigated the work hardening of Cu/Nb multilayers by room temperature rolling and pointed out that while the initial yield strength of a Cu/Nb multilayer with $h = 30$ nm is nearly two orders of magnitude greater than bulk Cu, the strength increment following strain hardening to unit strains is about the same ($\sim$300–350 MPa). The strain hardening exponent is lower in nanolayered materials compared with their bulk coarse-grained monolithic constituents, indicating a slightly reduced work hardening capacity in the nanolayered metals. In the rolled Cu/Nb multilayers with constant h no dislocation cell structure forms. The observed relative work hardening rates in nanolayered Cu/Nb may be interpreted in terms of glide dislocation interactions with interface dislocations, allowing cross-slip and annihilation related recovery processes [42]. Detailed analysis, however, is still needed to investigate the work hardening rates in metallic nanolayers. Recently Dayal et al. [27] show that the deformation behavior of Al/Pd micropillars (diameter $\sim$ 900 nm) exhibits a transition from dislocation driven plasticity at large h ($h > 40$ nm) to shear due to grain rotation via grain boundary sliding at small h ($h < 10$ nm). The strain hardening/softening behavior of nanoscaled metallic multilayers is still a subject that needs systematic study. In this paper we have investigated the stress–strain curves of Cu/Zr nanolayer micropillars using microcompression tests with a flat ended nanoindenter. The layer thickness-dependent strain hardening/softening behavior and the distinct morphological evolution of multilayer pillars are qualitatively interpreted by considering the dislocation-based deformation mechanism vs. grain boundary-mediated deformation mechanism, operating at different length scales.

2. Experimental procedures

2.1. Cu/Zr multilayer synthesis and microstructure characterization

Cu (99.995%) and Zr (99.99%) targets were used to deposit Cu/Zr multilayers on a hydrofluoric acid etched Si (1 0 0) substrate by direct current (d.c.) magnetron sputtering at room temperature. The chamber was evacuated to a base pressure of $\sim 6.0 \times 10^{-8}$ torr prior to sputtering, and 1.0–2.5×10^{-3} torr Ar was used during deposition. The substrate was neither heated nor cooled during deposition. The deposition rates were $\sim$1.1 nm s^{-1} for both Cu and Zr. The constituents within the Cu/Zr multilayers have equal individual layer thicknesses h, varying from 5 to 100 nm. The total thickness of the Cu/Zr multilayers was $\sim$1.6 μm. X-ray diffraction (XRD) experiments were performed in a Bruker D8 Discover X-ray powder diffractometer. High resolution transmission electron microscopy (HRTEM) and energy dispersive X-ray (EDX) analyses to identify the elemental composition and the interface integrity of the specimens were performed in a JEOL-2010 F microscope operated at 200 keV, with a Fischione ultra-high resolution high angle annular dark field detector (0.23 nm resolution in STEM image mode) and Oxford instruments EDX detector with a spatial resolution of $\sim$1 nm for chemical analysis.

2.2. Fabrication of Cu/Zr micropillars

The Cu/Zr multilayered micropillars, $\sim$600 nm in diameter (ϕ) with the interface planes perpendicular to the cylinder axis, were fabricated by the focused ion beam (FIB) technique using a Ga ion beam in a Helios 600 Dual Beam instrument, which also allows scanning electron microscopy (SEM) imaging. The expected aspect ratio (height to diameter) of the pillars was $\sim$3:1 to avoid buckling of the sample during compression [43]. The micropillar preparation process consisted of two steps, following the approach proposed by Greer et al. [13]. The first step was milling a ring of outer diameter 30 μm and inner diameter 10 μm. Second, a series of lower currents along with smaller concentric etched circles were used to obtain the final dimensions of the pillars. Currents as low as 28 pA were used to minimize any damage due to the Ga ion beam and to clean any redeposited material from the pillar surface. Note that we did not apply a protective coating layer to avoid any contribution to the mechanical response by foreign layers. The dimensions of the micropillars and the taper were measured by SEM. The aspect ratio (pillar height/diameter, β) of the pillars was about $\sim$2.9, while the taper of the pillars was between 2° and 4°.

In order to further reveal the effect of sample size or extrinsic size (pillar diameter) on the deformation behavior

pillars with different diameters of $\phi = 300$ ($\beta \sim 5.7$) and 800 nm ($\beta \sim 2.1$) were also fabricated for two representative Cu/Zr multilayers with $h = 5$ and 100 nm, using the method mentioned above.

2.3. Flat punch compression test

The microcompression test was performed in a Hystron Ti 950 with a 10 μm side flat quadrilateral cross-section diamond indenter. The tip–pillar alignment was undertaken with the aid of an optical microscope. All the micropillars were compressed under displacement controlled mode at a loading rate of $\sim$0.35 nm s^{-1} (corresponding to a constant strain rate of 2×10^{-4} s^{-1}) up to 15–30% strain, followed by holding for 5 s prior to unloading. Force–displacement data were continuously recorded and the engineering stress–strain curves were then calculated using the initial geometry of the pillar, as measured from the SEM images. The cross-sectional area at half height of the pillar (A_0) and the initial height (L_0) were used for calculations. However, in the pillar compression test in a nanoindenter the strains in the sample are estimated from the measured displacement of the indenter tip rather than directly from the sample. Thus, reducing the raw load–displacement data to engineering stress–strain curves gives modulus values that are too low, since the displacement measure includes compression of the base or substrate of the pillar. An attempt was made to correct for the compliance of the base of the pillar by using the model of a perfectly rigid circular flat punch being indented onto an isotropic half space first proposed by Sneddon [44], and used by various researchers (see Greer et al. [13], Singh et al. [28] and Lee et al. [45]). After obtaining the true compliance of the pillar the "corrected" load–displacement curves were obtained, then the engineering stress–strain curves were converted into true stress–strain curves using the homogeneous deformation model (assuming no volume change during deformation [5,13,45] and the final height and average cross-sectional area are L_p and A_p, respectively, such that $L_0A_0 = L_pA_p$). Following the treatment in Han et al. [5], Greer et al. [13], and Lee et al. [45] the true strain ε_T and true stress σ_T can be expressed as:

$$\varepsilon_T = \frac{1}{E}\frac{PL_p}{A_0L_0} + \ln\left(\frac{L_0}{L_p}\right) \tag{1}$$

and

$$\sigma_T = \frac{P}{A_p} = \frac{PL_p}{A_0L_0} = \frac{P}{A_0L_0}\left\{L_0 - \left[u_{tot} - \frac{\pi P(1-v_m^2)}{2E\sqrt{A_p}}\right]\right\} \tag{2}$$

where P is the load, E is the modulus of the Cu/Zr multilayers calculated from the rule of mixtures, u_{tot} is the total displacement, v_m is the Poisson's ratio of the multilayers ($\sim$0.33). At this point it should be noted that only homogeneous deformation is considered in the above calculations, while inhomogeneous deformation has frequently been observed in the compressive testing of both single crystalline micropillars [3,45,46] and nanostructured multilayer pillars [3,5]. Han et al. [5] have made an attempt to account for the softening-induced inhomogeneous deformation in Al/Al_3Sc multilayers by suggesting a constitutive equation to relate the yield strength directly to the strain softening parameter. However, the softening was experimentally found to occur after $\sim$10% strain in Al/TiN [3] and Cu/Nb [1] nanolayered pillars. This means that the deformation under 10% strain could be simply regarded as homogeneous, and the work hardening parameter derived from the above true stress–strain curves could be approximately used to investigate the size effect (both intrinsic and extrinsic) on the deformation behavior of nanolayered pillars.

3. Results

3.1. Microstructure of Cu/Zr multilayers

XRD results revealed that all Cu/Zr multilayers have a polycrystalline structure with (1 1 1) texture in the Cu layers and (0 0 0 2) texture in the Zr layers, as shown in Fig. 1. At smaller h the Cu (1 1 1) and the Zr (0 0 0 2) peaks broaden. In addition, both the Cu (1 1 1) and Zr (0 0 0 2) peak do not shift compared with the equilibrium state, which suggests that the Cu/Zr multilayer possesses opaque interfaces that are incoherent. TEM experiments were carried out to examine the modulated layer structure and interfaces in the multilayers. A typical cross-sectional view of the $h = 20$ nm Cu/Zr multilayers is displayed in Fig. 2a, which shows a chemically modulated layer structure. The selected area diffraction pattern (SADP) shows strong Cu (1 1 1) and Zr (0 0 0 2) texture. No significant intermixing between Cu and Zr was observed, as proved by both the interface HRTEM (Fig. 2b) and mapping analysis (Fig. 2c and d) of the Cu/Zr multilayers, with columnar grains in the Cu layers and nanocrystals in the Zr layers. There is no evidence of amorphization along the interfaces. The inverse fast Fourier transform (IFFT) HRTEM image for the Cu/Zr interface also revealed that the interface is incoherent, as shown in the inset in Fig. 2b.

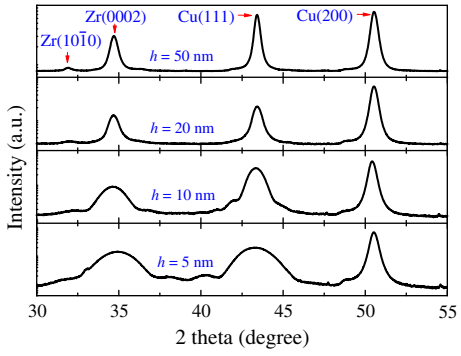

Fig. 1. XRD patterns of as-deposited Cu/Zr multilayers deposited on Si (1 0 0) substrates reveal strong Cu (1 1 1) and Zr (0 0 0 2) texture. The Cu (2 0 0) peak is observed in all specimens due to the use of a $\sim$100 nm Cu seed layer.

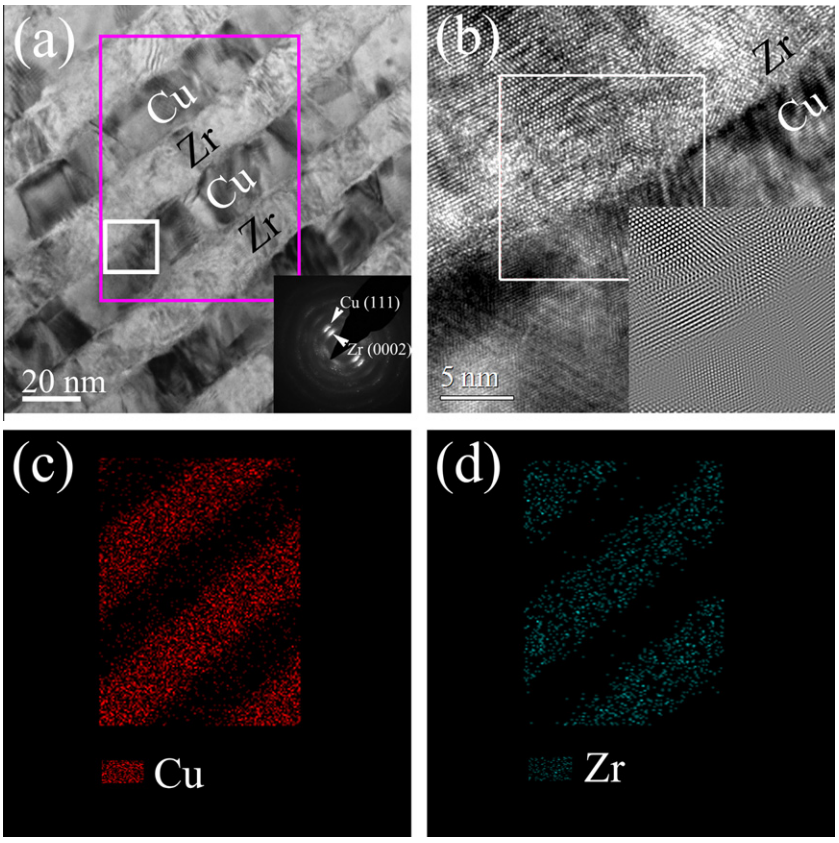

Fig. 2. (a) Bright field cross-sectional TEM micrograph showing the microstructure of the $h = 20$ nm Cu/Zr multilayers. (Inset) The corresponding selected area diffraction patterns (SADP). (b) HRTEM images typically showing the Cu/Zr interface of the white square boxed area in (a). (Inset) The inverse fast Fourier transform (IFFT) HRTEM image of the white squared box region, showing incoherent Cu/Zr interface. (c and d) Energy mapping analysis of the magenta rectangle region in (a) showing the chemical modulation structure with (c) Cu layers and (d) Zr layers.

3.2. Deformation behavior of Cu/Zr micropillars

Fig. 3a–h compares FIB/SEM images taken before and after uniaxial compression of multilayer micropillars with h of 100, 50, 20 and 5 nm, and a pillar diameter of 600 nm. Fig. 3a and b shows that when $h = 100$ nm the deformed pillar shows plastic barreling and extrusion of material from the individual Cu layers. In contrast, when $h = 20$ and 5 nm the pillars show shear deformation across the compression plane without significant barreling or extrusion. Both barreling (accompanied by extrusion) and shearing are observed in pillars with $h = 50$ nm. The length scale-dependent transition of deformation mode is similar to that of Cu/Nb nanolaminated composites rolled at room temperature [47] and compressed Al/Pd micropillars [27], demonstrating a significant intrinsic size effect.

In contrast, the extrinsic size effect (or sample size effect) on the deformation behavior is insignificant, compared with the intrinsic size effect. As shown in Fig. 4, the deformation mechanism remained unchanged when the diameter of the pillars varied from 800 to 300 nm. All the Cu/Zr pillars with $h = 100$ nm show the same deformation behavior of plastic barreling and extrusion of Cu layers, which was insensitive to the pillar diameter ($\phi = 300$ (Fig. 4c), 600 (Fig. 3b), and 800 nm (Fig. 4d)). All the 5 nm Cu/Zr pillars of various diameters deformed by shearing.

A comparison of the evolution of the morphology indicates that the intrinsic size effect is the dominant factor controlling the deformation behavior as the layer thickness is much smaller than the sample size. Nevertheless, the strength of certain multilayers appears sensitive to the pillar diameter, in particular for the Cu/Zr pillars with $h = 5$ nm, which will be addressed later.

3.3. True stress–strain curves of Cu/Zr micropillars

The compressed pillars were examined by SEM to confirm that the pillars had been compressed uniaxially without buckling or bending. Fig. 5a shows typical force–displacement curves for the above micropillars. When $h = 100$ nm the force acting on the pillar increased linearly with increasing displacement, followed by a smooth plastic deformation region, in agreement with the corresponding SEM images of the micropillars (Figs. 3b and 4b and d), in which barreling of the micropillar and extrusion of material from the individual Cu layers are observed. However, as h decreases to below 50 nm the force–displacement curves exhibit maxima different from those of 100 nm Cu/Zr pillars.

The calculated true stress–strain curves are shown in Fig. 5b. All the pillars showed three regimes of deformation. In regime I the curves showed a linear elastic behavior until the first yield point (σ_0) is reached ($\varepsilon = 0.02$–0.04).

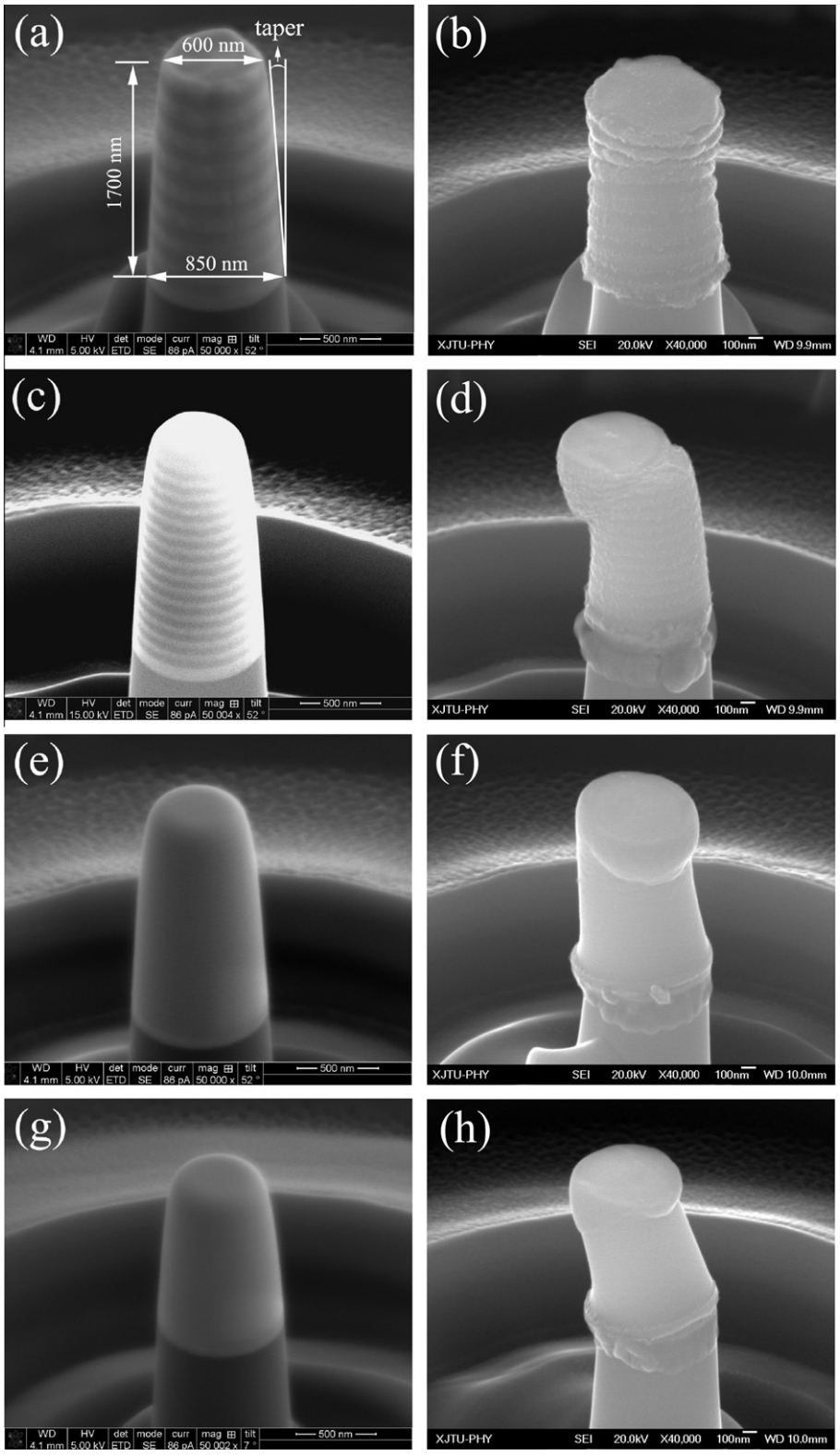

Fig. 3. SEM images of the $\phi = 600$ nm Cu/Zr micropillars with three different h, before and after the uniaxial compression tests. As-milled micropillar with (a) $h = 100$ nm, (c) $h = 50$ nm, (e) $h = 20$ nm and (g) $h = 5$ nm; (b) $h = 100$ nm micropillar after compression showing barreling of the micropillar and extrusion from individual Cu layers; (d) $h = 50$ nm micropillar after compression showing squeezing and shearing of the pillar; (f) $h = 20$ nm and (h) $h = 5$ nm micropillar after compression showing shearing of the micropillar.

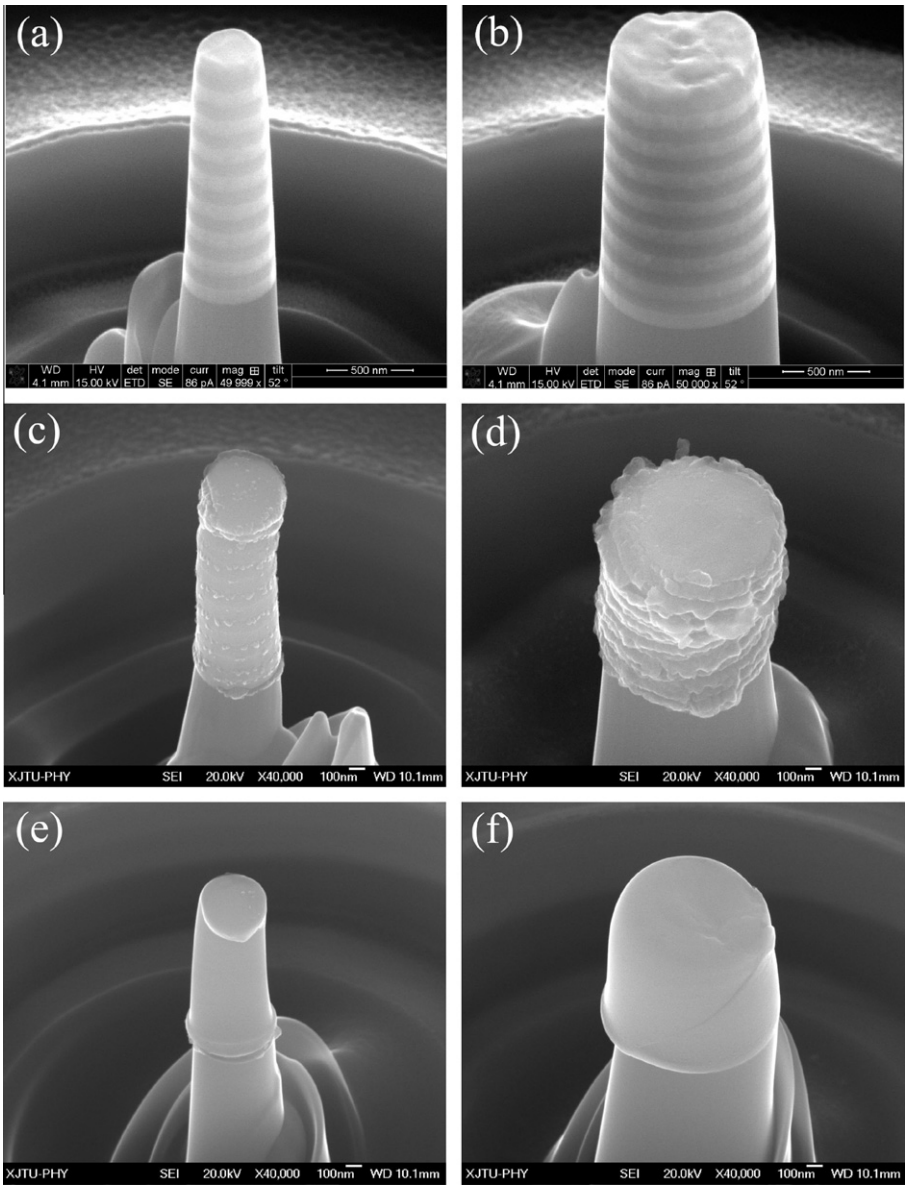

Fig. 4. SEM images of the Cu/Zr micropillars with two different ϕ, before and after the uniaxial compression tests. As-milled $h = 100$ nm micropillar with (a) $\phi = 300$ nm, (b) $\phi = 800$ nm; (c) $\phi = 300$ nm and (d) $\phi = 800$ nm micropillar with $h = 100$ nm after compression showing barreling of the micropillar and extrusion from individual Cu layers; (e) $\phi = 300$ nm and (f) $\phi = 800$ nm micropillar with $h = 5$ nm after compression showing shearing of the micropillar.

Regime II, spanning a strain level of ~0.05–0.1, shows strain hardening behavior, which can be described by Ludwik's equation [48]:

$$\sigma = K_1 + K_2\varepsilon_p^n \tag{3}$$

where K_1 represents the initial yield stress, K_2 is the strengthening coefficient (i.e. the strength increment due to strain hardening at plastic strain $\varepsilon_p = 1$), and n is the strain hardening exponent. Using Eq. (3) and taking $K_1 = \sigma_0$ we fitted the true stress–strain curves in regime II, as shown in Fig. 6a. The n values determined for all the pillars decrease as h is reduced, as shown in Fig. 6b. For example, n for $h = 20$ and 100 nm is ~0.39 and 0.52, respectively.

The strain hardening rate θ in this regime can be estimated using the equation:

$$\theta = \frac{d\sigma}{d\varepsilon} = \frac{n(\sigma_p - \sigma_{0.2\%})}{(\varepsilon_p - \varepsilon_{0.2\%})} = \frac{n\Delta\sigma}{\Delta\varepsilon} \tag{4}$$

The θ–ε_p curves for all the micropillars are shown in Fig. 6c, from which one can see that θ monotonically increases with decreasing ε_p and that the $h = 20$ nm micropillar always exhibits the maximum θ at a given ε_p. Taking $\Delta\sigma = \sigma_{2\%}$–$\sigma_{0.2\%}$ and $\Delta\varepsilon = 1.98\%$, the dependence of θ on h is shown in Fig. 6d. θ first increases with decreasing h, followed by a peak at a critical layer thickness h^{crit} of ~20 nm. A similar trend is also observed for $\Delta\sigma$. In regime

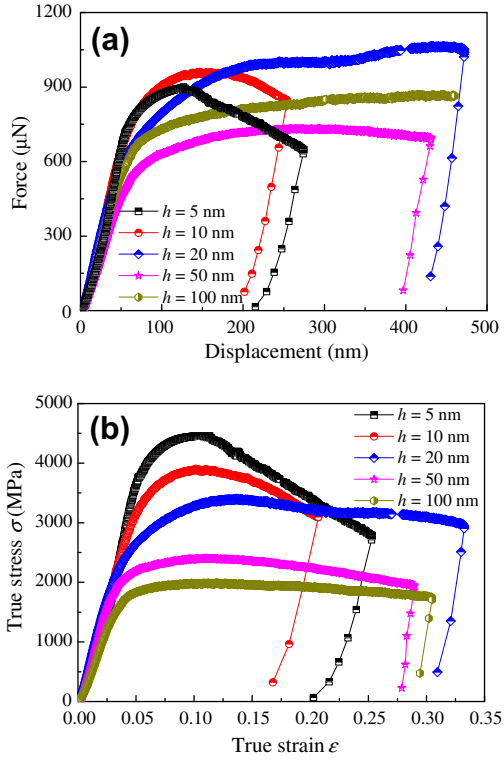

Fig. 5. (a) Force–displacement plots as a result of the uniaxial compression tests of the $\phi = 600$ nm Cu/Zr micropillars with five different h. (b) Corresponding true stress–strain plots for the $\phi = 600$ nm Cu/Zr micropillars with five different h.

III, at strains greater than ~0.1, strain softening is observed in the true stress–strain curves. As qualitatively revealed from the true stress–strain plots, there is a decrease in strain softening as h increases.

3.4. Strength of Cu/Zr micropillars

The plastic behavior of metals depends both on their physical size and microstructure (i.e. the "dimensional constraint" and "microstructural constraint", as discussed in Arzt [49]). Firstly, the initial yield strength $\sigma_{0.2\%}$ and the maximum strength σ_{max} (at $\varepsilon_p \approx 8\%$) were plotted against h, as shown in Fig. 7a. The strength values ($\sigma_{0.2\%}$ and σ_{max}) monotonically increase with reducing h. One can see that $\sigma_{0.2\%}$ rises slowly as h decreases to below 10 nm, while σ_{max} increases rapidly. This means that the intrinsic size effect on the strength of Cu/Zr pillars is notable.

Secondly, we plotted $\sigma_{0.2\%}$ against ϕ to identify the extrinsic size effects on pillar strength (see Fig. 7b). For $h = 100$ nm Cu/Zr pillars with plastic deformation and Cu extrusion $\sigma_{0.2\%}$ remains almost unchanged as ϕ decreased from 800 to 600 nm. Further reducing ϕ down to 300 nm increases $\sigma_{0.2\%}$ by only 10% (from about 1125 to 1250 MPa). For $h = 5$ nm Cu/Zr pillars $\sigma_{0.2\%}$ increased by more than 70%, from ~1550 to 2750 MPa as ϕ decreased from 800 to 600 nm. An ~10% increase in $\sigma_{0.2\%}$ is achieved when ϕ is reduced from 600 to 300 nm.

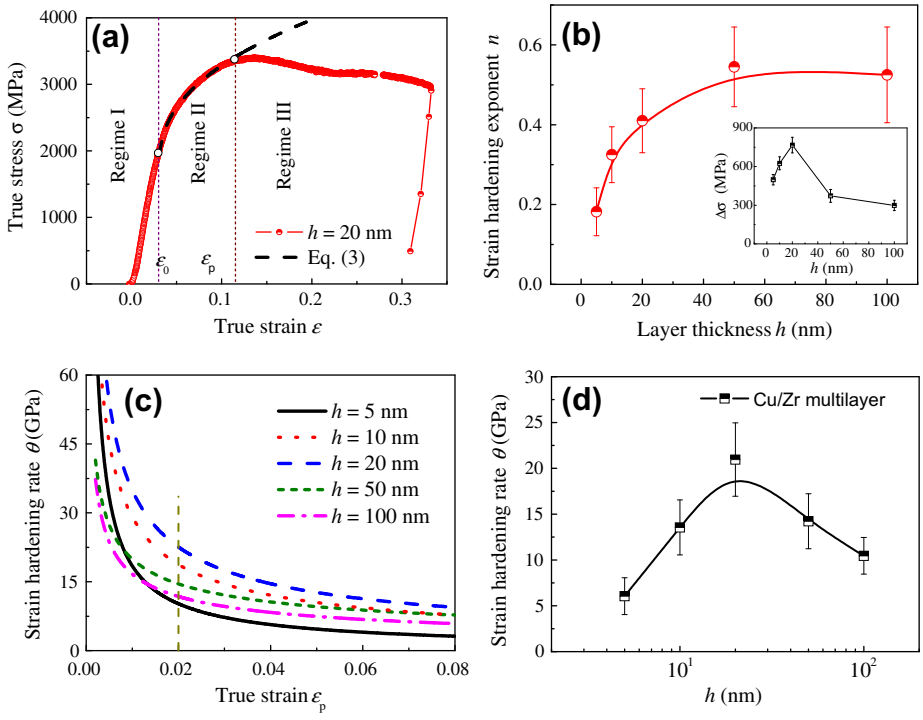

Fig. 6. (a) True stress–strain plot for $h = 20$ nm Cu/Zr micropillars with $\phi = 600$ nm loaded perpendicular to the layer interface. Note the degree of strain softening after a maximum stress of 3.37 GPa is reached. The strain hardening regime (regime II) is fitted using Eq. (3). (b) The strain hardening exponent n, and stress increment $\Delta\sigma$ (inset) as a function of h for $\phi = 600$ nm Cu/Zr micropillars. (c) Strain hardening rate θ–plastic strain ε_p curves for $\phi = 600$ nm Cu/Zr micropillars with five different h. (d) Strain hardening rate θ of $\phi = 600$ nm Cu/Zr micropillars as a function of h. The line is a guide to the eyes.

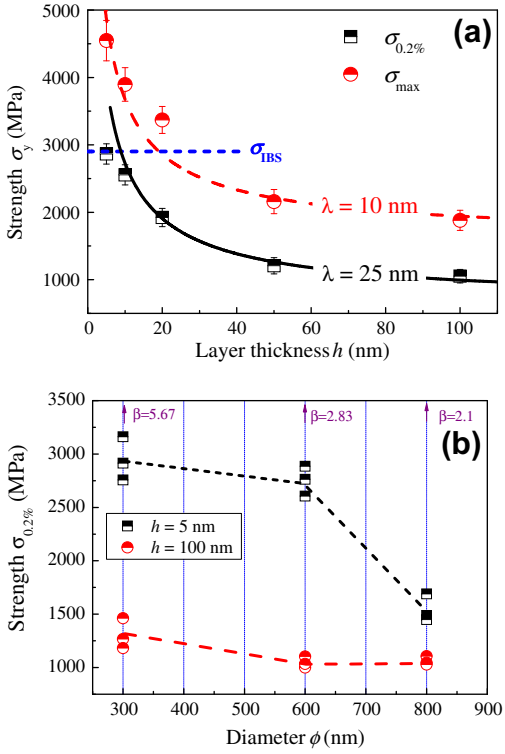

Fig. 7. (a) Strength of $\sigma_{0.2\%}$ and σ_{max} of $\phi = 600$ nm Cu/Zr micropillars plotted as a function of h. $\sigma_{0.2\%}$ and σ_{max} are both fitted using Eq. (7) and σ_{IBS} (dashed line) is calculated using Eq. (8). (b) Strength of $\sigma_{0.2\%}$ plotted as a function of ϕ for two representative Cu/Zr micropillars with $h = 5$ nm and 100 nm, respectively.

4. Discussion

4.1. Deformation mechanism of Cu/Zr micropillars

When $h = 100$ nm SEM micrographs show that the soft Cu layer thins and is preferentially squeezed out from between the Zr layers due to the strength disparity between Cu and Zr, and plastic barreling takes place, which is analogues to that of amorphous/crystalline CuZr/Cu pillars [6] and crystalline/crystalline Al/Pd pillars [27] deformed under compression. This is expected, as the base of the pillar is fixed and friction occurs between the top mating surface of the pillar and the indenter. The amount of barreling increases with the load applied. The taper in the pillar produces higher local stresses at the top where the cross-sectional area is smaller [28]. This depth-dependent stress gradient also leads to more localized deformation in the Cu layer at the top of the tapered micropillars (see Figs. 3b and 4b and d). This feature may be unique to the multilayer pillar as this was not seen in several single phase metallic pillars [14–16]. This deformation process (when $h \geqslant 50$ nm) can be understood with the assistance of the schematic in Fig. 8. Cu flows plastically between the Zr layers. The plastic flow of the soft Cu is constrained by the harder Zr layers, because mobile dislocations in the Cu layers are deeply pinned by the interfaces. The Zr layers cannot be compressed beyond a certain point, due to the Cu layers in between them. Thus a mutual constraint exists between the hard Zr and soft Cu layers in the multilayers, which contributes to the very high strength observed for these materials [28].

It should be pointed out that to deformation of Cu within each layer appears uniform without evidence of shear localization. The applied load will exert equal resolved shear stresses on the {1 1 1} planes A (A-P) and B (B-P), with no shear stress on planes C (C-P), which is also the interface plane (see Fig. 8a). With symmetrical slip activity of a single dislocation [50] on A-P and B-P and no resolved shear stress on C-P plastic flow is expected to be stable, resulting in uniform thinning of the layers and no rotation of the interface plane due to the interface barrier strength (IBS) $\sigma_{IBS} > \sigma_{max}$ (discussed below), as observed in the case of rolled Cu/Nb nanolayered composites [47,50,51]. However, one can see that the thickness of the Zr layers is not significantly reduced (compare Fig. 3a with b). This is because Zr with a grain size of ~30–50 nm may have a much higher strength than the soft nanocrystalline Cu layer. For example, bulk nanocrystalline Cu with an average grain size of 30 nm has a strength of ~1.2 GPa [6], while nanocrystalline Zr (~30 nm in grain size) exhibits a strength of 2.6–3 GPa [24].

In contrast, in micropillars with $h = 20$ nm and below barreling of the micropillar is evident, accompanied by localized shear deformation initiated at geometric stress concentrators, such as pillar corners. Shear failure of micropillars is also observed in $h = 10$ nm Al/Pd micropillars [27]. Meanwhile the smooth surface of compressed Cu/Zr pillars shows that Cu was not squeezed out, as observed in thicker multilayers. These indicate that different deformation mechanisms may be operating in micropillars with smaller h ($\leqslant$20 nm). At this length scale ($h = 5$–20 nm) the confined layer slip (CLS) of dislocations in the Cu layers can still operate [40,52,53]. At low strain multiple slip systems are activated with balanced slip activity such that the net out of plane rotation is negligible. This results in a uniformly spaced slip distribution and, hence, a uniform reduction in layer thickness [47,54]. However, at higher plastic strains (>5%), $\sigma_{IBS} < \sigma_{max}$ (discussed below), the net out of plane rotation may increase due to the transmission of dislocations across the layer interface. On the other hand, the grain size of Zr (d_{Zr}) is so small ($d_{Zr} = 4$–12 nm) that GB-mediated deformation [55–57] (grain rotation and GB sliding) plays a dominant role in the compressibility of $h \leqslant 20$ nm micropillars and probably contributes to the catastrophic failure by shear localization. Hahn et al. [58] pointed out that once a planar interface is formed localized sliding shear can result in macroscopic sliding over the dimensions of many grains and eventually lead to a large strain based on the GB sliding mechanism, which was subsequently proved in a deformed nanocrystalline metal (Pd) [59]. Jang and Greer [22] also found that a GB-mediated mechanism occurred in 60 nm grained nanocrystalline Ni–W nanopillars by performing in situ uniaxial tension and compression experiments. Based on these results we suspect that the

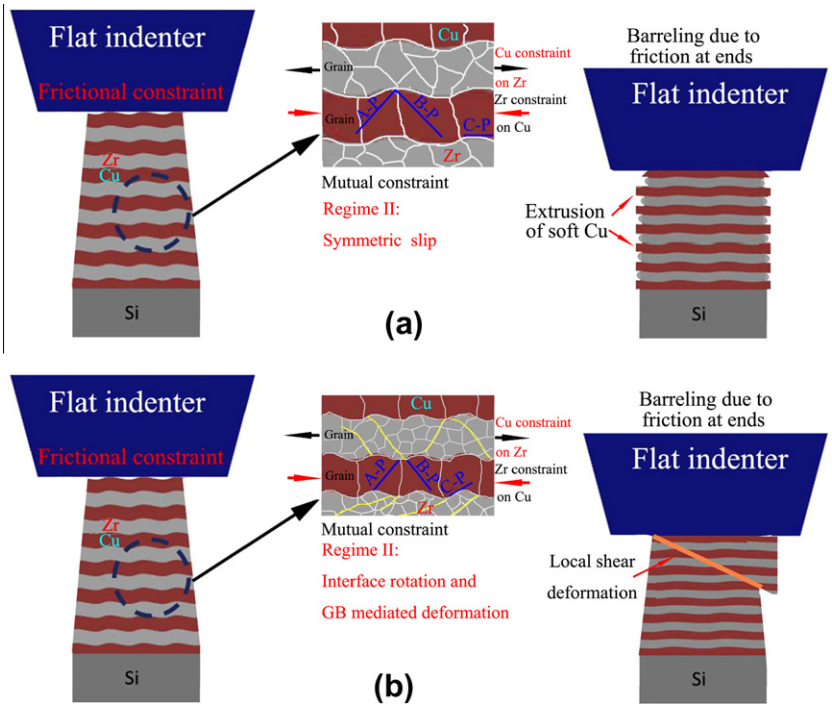

Fig. 8. Schematic of (a) symmetrical slip-induced uniform deformation mechanism at larger h and (b) interface rotation and GB mediated deformation-induced shear deformation mechanism at smaller h in Cu/Zr micropillars during compression testing. Both Cu and Zr are mutually constrained. Plastic deformation of the Cu layer results in squeezing out of Cu on the free face of the micropillar in (a). Yellow lines represent the mesoscopic glide planes in the Zr layers in (b). (For interpretation of the references to color in this figure legend, the reader is referred to the web version of this article.)

deformation of micropillars with $h \leqslant 20$ nm is controlled by a dislocation-based mechanism in the Cu layers and grain rotation (via GB sliding) in the Zr layers stimulating shear deformation (see Fig. 8b). At smaller h ($\leqslant$20 nm) the strength of Cu increases continuously with decreasing h, and consequently leads to co-deformation of Cu and Zr [6,54] and suppression of the preferential thinning of the Cu layers due to extrusion. When $h = 50$ nm both the squeezing of Cu and shear localization of the pillars are observed, indicating a combination of conventional dislocation-based plasticity and grain rotation initiated shear localization. Another striking feature is that, for pillars of various diameters, 5 nm Cu/Zr multilayer pillars exhibit shear deformation, whereas 100 nm Cu/Zr pillars show uniform thinning of the Cu layers. This observation indicates that the deformation mode is dominated by the intrinsic size effect in the present size ranges.

4.2. Strain hardening–softening behavior

Low strain hardening has hitherto been considered an intrinsic behavior for most nanostructured materials (e.g. nanocrystalline metals) [48,60,61], due to their perceived inability to accumulate dislocations. Strikingly, the present study has shown that nanostructured multilayers can sustain the highest work hardening capability (and work hardening rate) at or somewhat above a critical size. Most recently it has been reported that cryogenically rolled nanocrystalline Ni with a grain size of ~20 nm showed strong strain hardening under large plastic strain, owing to significant dislocation accumulation in the grain interior, which is enabled primarily by Lomer–Cottrell locks through pinning of lock-forming dislocations and obstruction of dislocation motion [62]. On the other hand, in situ tensile testing of 30 nm Cu/60 nm Ni multilayers proved that as the nucleated dislocations (from GB and interfaces) encountered a boundary they spread laterally within the layer until the dislocation saturated the glide plane, forming pile-ups [52]. Furthermore, in situ nanoindentation testing of 5 nm Al/Nb multilayers [63] demonstrated that dislocation activity remains abundant inside the crystal lattice and the dislocation density is as high as $\sim 10^{16}$ m^{-2}, which indicates preferential storage of dislocations at the interface (or the dislocations are absorbed by the interface), which should account for the large magnitude of plastic deformation in these crystals. This evidence suggests that abundant dislocations can accumulate and be stored in the grain interiors and/or inside the layers during deformation.

Misra and co-workers [64] presented a simple analysis that allowed limiting values at which these different mechanisms operate on the microstructural scale to be obtained and gave a "deformation mechanism map" for polycrystalline multilayers describing dislocation-based (continuum and discrete) pile-up or non-pile-up mechanisms, and non-dislocation type deformation modes. It was found that at larger misfits the pile-up region would shift to lower values of d (grain size) and h (layer thickness), scaling almost linearly with the misfit strain [64]. For Cu the critical layer

thickness for continuum pile-up $h_c = 16$ nm for a misfit of 2.5% and 4 nm for a misfit of 10.5%, at which the number of dislocations in the screw pile-up is 2 [52,64]. In our case of a Cu/Zr multilayer the misfit strain between Cu (1 1 1) and Zr (0 0 0 2) is even larger than 10.5%, which gives $h_c < 4$ nm. Thus for nanolayered metals continuum-scale dislocation pile-up is not completely suppressed, as the dislocation source to obstacle distance (typically of the order of $h > 5$ nm) is large enough to accommodate numerous dislocations on a glide plane against an obstacle (i.e. interface). The CLS in both layers on multiple slip systems can introduce sets of dislocations with the full Burgers vectors of Cu or Zr that may be oriented on the respective glide planes or in the interface plane, and create residual dislocations with Burgers vector b_{Cu}–b_{Zr} at the interface [42]. The incoherent Cu/Zr interface may have a low shear strength similar to Cu/Nb and, hence, strong barriers to slip transmission due to dislocation core spreading along the weak interfaces [8,65,66]. Above h^{crit} ($h^{crit} < h < 100$ nm) the plastic flow is initially confined to one layer and occurs by glide of a single dislocation in the form of hairpin-shaped dislocation loops propagating within a layer. The stress to propagate the single dislocation loops $\sigma_{Loop} < \sigma_{IBS}$ is a necessary condition for the confinement of glide loops within layers. Here σ_{Loop} for 60° dislocations in Cu can be expressed as [3,40]:

$$\sigma_{Loop} = M\frac{\mu^* b}{8\pi h'}\left(\frac{4-\nu}{1-\nu}\right)\ln\frac{\alpha h'}{b} \quad (5)$$

where M is the Taylor factor, $h' = h/\sin\varphi$ is the layer thickness parallel to the glide plane, φ is the angle between the slip plane and the interface, b is the magnitude of the Burgers vector, ν is the Poisson ratio for Cu, $\mu^* = (\mu_{Zr}\cdot\mu_{Cu})/(V_{Zr}\cdot\mu_{Cu} + V_{Cu}\cdot\mu_{Zr})$ is the effective shear modulus of the Cu/Zr multilayers, which can be estimated from the shear modulus μ_{Cu} and volume fraction V_{Cu} of the Cu layer and those of the Zr layer, and α represents the core cut-off parameter, varying from 0.2 (for a compact core) to 1 (for a spread core). Although σ_{Loop} scales (primarily) with the modulus of the layer and $h^{-1}\ln(h/b)$, it is not high enough to promote the cross-slip of dislocations [8,67,68]. On the other hand, the Cu/Zr interfaces are incoherent even for layer thicknesses of the order of several nanometers (see the XRD and HRTEM results). This implies that the interfacial structure does not change significantly with h from several to a few tens of nanometers. Therefore the IBS, σ_{IBS}, which is characteristic of a given interface, is expected to remain constant at this length scale.

However, as h decreases further ($h < h^{crit} = 20$ nm) σ_{Loop} must increase (but still be less than σ_{IBS}) to ensure that the dislocation loops propagate and can overcoming the resistance to movement from interface dislocations. Under this condition cross-slip is a relatively easy way to achieve deformation and the dislocations gliding on slip plane I can be stimulated to glide on slip plane II (see Fig. 9), which does not require the glide dislocations to overcome the repulsion by orthogonal dislocations at a stand-off distance [68]. Thus dislocation cross-slip would lower the strain hardening ability, operating on small length scales ($h < 20$ nm) [42,69].

The inverse layer thickness (or grain size) effect reported here has also been observed in both unpassivated and passivated Cu films with thickness range spanning from 20 to 800 nm [70]. Below h^{crit} the strain hardening rate θ decreases with reducing h while above h^{crit} a smaller h leads to higher θ, similar to coarse–ultrafine grained pure metals (e.g. Cu [71–73]), as shown in Fig. 6d. These suggest that below and above $h^{crit} \approx 20$ nm the nanolayered micropillars exhibit different strain hardening abilities, which can probably be explained in terms of the ability of favorably oriented dislocations to cross-slip [68,74,75]. Above h^{crit} dislocation motion in the form of pile-up on multiple slip systems results in the formation of Lomer–Cottrell type barriers created by intersecting dislocations from different slip systems and/or dislocation tangles and dislocation cell structures. While below h^{crit} dislocation cross-slip can occur due to the relative lower stress needed to drive dislocation motion.

In regime III, where strain softening occurred, Ludwik's equation cannot be used to fit the true stress–strain curves (see Fig. 6a). The monotonically increasing strain softening with reducing h may be partially supported by the continuously reducing n (see Fig. 6b). A possible explanation is that the dislocations are transmitted across the interfaces in samples with the smallest h, leading to softening [5]. Once the dislocations start to shear through the Cu layers it is likely that the Zr layer will no longer act as a strong barrier to dislocation movement, and softening of the deformed volume will occur. However, the strength of the multilayers in the single dislocation-based continuum pile-up regime will typically be determined by the lower of the following two estimates: (i) the critical stress needed to push a glide dislocation through the interface [8,67,76]; (ii) the stress σ_{Loop} to propagate the single dislocation loops [40,53,77]. The observation of increasing strength with decreasing h on the few nanometer length scale indicates that the strength of multilayers on such a length scale is determined by confined layer bowing of single dislocations. Softening is probably caused by other mechanisms, such as shear band formation [1]. Indeed, in Cu/Zr multi-

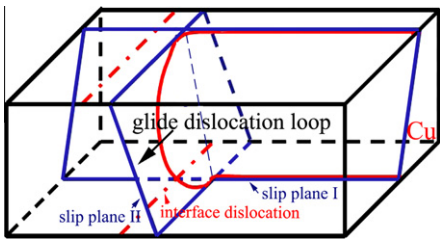

Fig. 9. Schematic illustration of a glide loop on slip plane I, due to repulsion from the orthogonal interface dislocations, cross-slip on slip plane II moving parallel to the obstacle interface dislocations in Cu/Zr multilayers, which would produce less work hardening. Multiple slip systems would be active in Cu layers, even though only one system is shown in the Cu layer.

layers more severe shear deformation and stain softening are observed in micropillars with smaller h. Since the Cu/Zr interfaces are incoherent and may be weak in shear, the resolved shear stress on the interface plane due to layer rotation may be sufficient to facilitate interfacial slip [8,78]. Since the interface plane may be relatively weak compared with the slip planes within the layer, slip on the interface plane may be preferred over intralayer slip. Continued shear along the interface at stresses much lower than those needed to have slip on intralayer systems is the onset of geometric softening [1], which could be operative at high stresses (strains). Consequently strain softening is exhibited by these materials at high strains. Deformation at low strain may also restore a large number of dislocations and facilitate subsequent work softening [79,80], which is probably true for the case of $h = 100$ nm micropillars. In parallel, GB-mediated deformation in the Zr layers can also contribute to shear deformation via formation of mesoscopic glide planes [27].

4.3. Scaling behavior of strength

As previously pointed out, CLS could still operate on the present length scales where continuum dislocation pile-ups can form. Eq. (5) represents the CLS stress to propagate a single dislocation in the absence of strain hardening. In fact, the interface may already have one or more arrays of misfit dislocations that will act as obstacles to CLS. CLS also leads to multiple dislocation segments being deposited at the interfaces. As a hairpin dislocation loop begins to glide in a confined metal layer it interacts with dislocation segments deposited at the interface as a result of other CLS loops. In general there will be a dislocation array at the interface that is parallel to the trace of the CLS loop on the interface and others that are oblique to it. These glide dislocation–interface dislocation interactions can result in significant stain hardening, which can be expressed as [3]:

$$\sigma = \frac{\mu b}{\lambda(1-\nu)} \tag{6}$$

where λ is the spacing of a parallel array of glide dislocation loops. In addition, the interfaces have a characteristic interface stress (f) that arises from elastic deformation of the interfacial region and assists the applied stress for CLS by of the order of f/h [40]. Thus by considering the effects of dislocation interactions (strain hardening) and interface stress on the CLS stress σ_{Loop}, the applied stress σ_{CLS} required to propagate a glide loop with Burgers vector b confined to one Cu layer is:

$$\sigma_{\text{CLS}} = M\frac{\mu^* b}{8\pi h'}\left(\frac{4-\nu}{1-\nu}\right)\ln\frac{\delta h'}{b} + \frac{\mu b}{\lambda(1-\nu)} - \frac{f}{h} \tag{7}$$

where f is the characteristic interface stress of the multilayer, typically $f = 2$–3 J m^{-2} [40], and all the other symbols have the same meaning as mentioned above. With a series of parameters $M = 3.06$, $\mu^* = 40.6$ GPa, $\nu = 0.343$, $b = 0.2556$ nm, $\alpha = 1$, $\varphi = 70.5°$ and $\lambda = 25$ nm (for $\sigma_{0.2\%}$ at $\varepsilon_p = 0.2\%$) the dependence of strength on h is calculated as shown in Fig. 7a, which agrees well with the experimental data for $h > 5$ nm. The calculated results somewhat overestimate the experimental value for $h = 5$ nm, indicating the transmission of dislocations across the interface instead of slip in the confined layer [40,53]. It is evident that the strength $\sigma_{0.2\%}$ for $h \leqslant 10$ nm increases slowly, while $\sigma_{\max}$ rises sharply. The difference in tendency of the length scale-dependent strength between $\sigma_{0.2\%}$ and $\sigma_{\max}$ is probably caused by strain hardening. In other words, at low strain (for $\sigma_{0.2\%}$) dislocation glide is confined in the Cu layer and dislocation–interface interaction is weak, nevertheless, at high strains (for $\sigma_{\max}$) the dislocation may cut cross the interface and induce significant strain hardening. Maaß et al. [81] pointed out that when using flow stress at 5% strain or higher the "smaller is stronger" paradigm observed for 1–10 μm fcc FIB pillars is to a great extent due to size-dependent strain hardening, i.e. the evolution of the microstructure during deformation, and not to a size dependence of the initial strength of the single crystal pillar. Thus one can see that the model also fits the data well for $\sigma_{\max}$ with $\varepsilon_p = 8\%$ and $\lambda = 10$ nm (corresponding to a dislocation density of the order of $\sim 10^{16}$ m^{-2}, which was observed in Al/Nb multilayers after an indentation test [63]).

An interfacial barrier to dislocation slip transmission is characteristic of interfacial structure and strongly influenced by lattice mismatch and shear modulus mismatch between the two constituent layers [67,82]. Hence, if the interfacial structure does not change with h, σ_{IBS} also remains independent of h, and is given by [67,82]:

$$\sigma_{\text{IBS}} = M\left[\xi\mu^*\left(\zeta - \frac{b}{\lambda}\right) + \frac{R\mu_{\text{Zr}}\sin\varphi}{8\pi}\right] \tag{8}$$

The first and second terms are the influence of misfit strain and the modulus effect on IBS, respectively, where ξ is Saada's constant, $R = (\mu_{\text{Cu}} - \mu_{\text{Zr}})/(\mu_{\text{Cu}} + \mu_{\text{Zr}})$, ζ is the lattice mismatch without taking account of the detailed crystallographic orientation at the interface [83], λ is a parallel array of spaced glide loops, and the other symbols have the same meaning as before. A total plastic strain of 5% in the pillar is equivalent to a plastic strain of ~10% in the Cu layers if it is assumed that all the plastic deformation is confined to the Cu layers. The in-plane plastic strain corresponding to a compressive plastic strain of 10% is equal to ~5%, assuming volume conservation. Taking $\varphi = 70.5°$, $\lambda = 7$ nm, $\zeta = 11\%$ and $\xi = 0.32$, and using Eq. (8), $\sigma_{\text{IBS}} \approx 2.9$ GPa (Fig. 7a), consistent with the strength of the present multilayers with $h = 5$ nm. It is suggested that for multilayers on large length scales ($h > 50$ nm) the nucleation and motion of dislocations is strongly limited within the confined layer even at high strains, which can result in homogeneous deformation with barreling and extrusion of Cu. For multilayers on small length scales ($h < 50$ nm) dislocation can cut cross the interface leading to shear deformation at high strains [47], consistent with the SEM observations.

4.4. Intrinsic size vs. extrinsic size effect on strength

In single crystals (pillar [14–16,23,84,85] and thin film [85–87]) the ultimate tensile strength and the yield strength scale with the external sample size in a power law fashion, sometimes attaining a significant fraction of the material's theoretical strength, and exhibiting the commonly known phenomenon "smaller is stronger". In contrast, both the intrinsic (i.e. microstructural) and extrinsic (i.e. sample size) dimensions play a non-trivial role in the mechanical properties and material deformation mechanisms in polycrystalline materials, therefore it is critical to understand their interplay and mutual effects on the mechanical properties and material deformation, especially in small-scale structures. The strength of polycrystalline metallic thin films is determined by the smaller microstructural dimensions between film thickness and grain size [88,89].

Mara et al. [1,2] fabricated and uniaxially compressed micron-sized Cu/Nb pillars with equal h of 5 and 40 nm and much larger pillar diameters between 4 and 8 μm. Almost no pillar size effect has been found within this diameter range [23], and the conjecture was made that the mechanical behavior and strength are fully controlled by the individual layer thickness, i.e. the intrinsic length scale, whereby individual dislocations transmit through the Cu/Nb interfaces, rather than by the pillar size [1,2,23]. This seems to be reasonable because the extrinsic size (ϕ) is over two orders of magnitude larger than the intrinsic size (h). However, a strong extrinsic size effect is observed in the present Cu/Zr multilayer pillars with $h = 5$ nm, where the pillar diameter is also two orders greater than the layer thickness. In the Cu/Zr multilayer pillars with $h = 100$ nm pillars the extrinsic size effect is not significant even though the pillar diameter is of the same level as the layer thickness. These demonstrate that (i) the sample size effect on the strength of multilayer pillars may be related to the deformation behavior, and (ii) a sample size effect on multilayer pillars is notable when the pillar diameter is below the submicron level.

Attention should also be paid to the effect of sample aspect ratio. The variation in sample diameter from 800 to 300 nm alters the sample aspect ration (β) from ~2.10 to 5.67, which may change the stress distribution and local deformation concentration in submicron pillars with shear deformation. Under uniform deformation it has been concluded [90] that there is no pronounced impact of the aspect ratio on the flow stress within the range $\beta = 2{:}1$ and 13.5:1. However, in the present Cu/Zr 5 nm pillars with inhomogeneous deformation (shear deformation) the strength increased rapidly at $\beta = 2.83$ (Fig. 7b). This is distinct from the case of uniform deformation. Further analyses are being performed to understand this discrepancy.

5. Conclusions

Systematic compression tests were performed on incoherent Cu/Zr multilayer pillars with layer thicknesses ranging from 5 to 100 nm, to examine length scale effects on the mechanical response of nanolayered materials. The following conclusions can be derived from this study.

1. The deformation mechanism of Cu/Zr micropillars transforms from preferential thinning (squeezing out) of Cu at larger h to shear localization at smaller h (<50 nm).
2. Work hardening initially increases with decreasing h, and achieves a maximum at $h = 20$ nm, followed by an inverse h dependence. More glide–interface dislocation interactions result in increasing θ with reducing h, below which dislocation cross-slip lowers θ, thus leading to an inverse h dependence of θ.
3. There was an increase in strain softening and a decrease in strain hardening at high strain as h decreases. The reduced stress can be attributed to interface rotation and dislocation-induced shear along the interface.
4. The CLS model is used to interpret the observed scaling behavior of strength. The calculations agree well with the experimental data, except for $h = 5$ nm at low strain, because of the transmission of dislocations across the interface instead of glide in the confined layer.

Acknowledgements

This work was supported by the 973 Program of China (Grant No. 2010CB631003), the 111 Project of China (B06025) and the National Natural Science Foundation of China (50971097). G.L. thanks the Fundamental Research Funds for the Central Universities for support and J.Y.Z. thanks the China Scholarship Council for financial support. X.Z. acknowledges financial support by the NSF-DMR Metallic Materials and Nanostructures Program, under Grant No. 0644835.

References

[1] Mara NA, Bhattacharyya D, Hirth JP, Dickerson P, Misra A. Appl Phys Lett 2010;97:021909.
[2] Mara NA, Bhattacharyya D, Dickerson P, Hoagland RG, Misra A. Appl Phys Lett 2008;92:231901.
[3] Bhattacharyya D, Mara NA, Dickerson P, Hoagland RG, Misra A. Acta Mater 2011;59:3804.
[4] Liu Y, Bufford D, Wang H, Sun C, Zhang X. Acta Mater 2011;59:1924.
[5] Han SM, Phillips MA, Nix WD. Acta Mater 2009;57:4473.
[6] Liu MC, Lee CJ, Lai YH, Huang JC. Thin Solid Films 2010;518:7295.
[7] Misra A, Kung H. Adv Eng Mater 2001;3:217.
[8] Wang J, Misra A. Curr Opin Solid State Mater Sci 2011;15:20.
[9] Was GS, Foecke T. Thin Solid Films 1996;286:1.
[10] Zhang JY, Zhang X, Wang RH, Lei SY, Zhang P, Niu JJ, et al. Acta Mater 2011;59:7368.
[11] Zhang JY, Zhang X, Liu G, Zhang GJ, Sun J. Scripta Mater 2010;63:101.
[12] Zhang JY, Liu G, Zhang X, Zhang GJ, Sun J, Ma E. Scripta Mater 2010;62:333.
[13] Greer JR, Oliver WC, Nix WD. Acta Mater 2005;53:1821.
[14] Uchic MD, Dimiduk DM, Florando JN, Nix WD. Science 2004;305:986.

[15] Uchic MD, Shade PA, Dimiduk DM. Annu Rev Mater Res 2009;39:361.
[16] Yu Q, Shan Z, Li J, Huang X, Xiao L, Sun J, et al. Nature 2010;463:335.
[17] Kim J-Y, Greer JR. Acta Mater 2009;57:5245.
[18] Schneider AS, Kaufmann D, Clark BG, Frick CP, Gruber PA, Monig R, et al. Phys Rev Lett 2009;103:105501.
[19] Kirchlechner C, Keckes J, Motz C, Grosinger W, Kapp MW, Micha JS, et al. Acta Mater 2011;59:5618.
[20] Norfleet DM, Dimiduk DM, Polasik SJ, Uchic MD, Mills MJ. Acta Mater 2008;56:2988.
[21] Kiener D, Guruprasad PJ, Keralavarma SM, Dehm G, Benzerga AA. Acta Mater 2011;59:3825.
[22] Jang D, Greer JR. Scripta Mater 2011;64:77.
[23] Greer JR, De Hosson JTM. Prog Mater Sci 2011;56:654.
[24] Liu MC, Huang JC, Chou HS, Lai YH, Lee CJ, Nieh TG. Scripta Mater 2009;61:840.
[25] Bei H, Shim S, Pharr GM, George EP. Acta Mater 2008;56:4762.
[26] Frick CP, Orso S, Arzt E. Acta Mater 2007;55:3845.
[27] Dayal P, Quadir MZ, Kong C, Savvides N, Hoffman M. Thin Solid Films 2011;519:3213.
[28] Singh DRP, Chawla N, Tang G, Shen YL. Acta Mater 2010;58:6628.
[29] Ng KS, Ngan AHW. Scripta Mater 2008;59:796.
[30] Shan ZW, Mishra RK, Asif SAS, Warren OL, Minor AM. Nature Mater 2007;7:115.
[31] Greer JR, Nix WD. Phys Rev B 2006;73:245410.
[32] Zhou C, Biner SB, LeSar R. Acta Mater 2010;58:1565.
[33] Dimiduk DM, Woodward C, Lesar R, Uchic MD. Science 2006;312:1188.
[34] Csikor FF, Motz C, Weygand D, Zaiser M, Zapperi S. Science 2007;318:251.
[35] Kocks UF, Mecking H. Prog Mater Sci 2003;48:171.
[36] Chen MW, Ma E, Hemker KJ, Sheng HW, Wang YM, Cheng XM. Science 2003;300:1275.
[37] Zhang JY, Liu G, Wang RH, Li J, Sun J, Ma E. Phys Rev B 2010;81:172104.
[38] Van Swygenhoven H, Derlet P, Froseth A. Acta Mater 2006;54:1975.
[39] Yamakov V, Wolf D, Phillpot SR, Mukherjee AK, Gleiter H. Nature Mater 2004;3:43.
[40] Misra A, Hirth JP, Hoagland RG. Acta Mater 2005;53:4817.
[41] Phillips MA, Clemens BM, Nix WD. Acta Mater 2003;51:3157.
[42] Misra A, Zhang X, Hammon D, Hoagland RG. Acta Mater 2005;53:221.
[43] Zhang H, Schuster BE, Wei Q, Ramesh KT. Scripta Mater 2006;54:181.
[44] Sneddon IN. Int J Eng Sci 1965;3:47.
[45] Lee S-W, Han SM, Nix WD. Acta Mater 2009;57:4404.
[46] Han SM, Bozorg-Grayeli T, Groves JR, Nix WD. Scripta Mater 2010;63:1153.
[47] Misra A, Hoagland RG. J Mater Sci 2006;42:1765.
[48] Lu L, Chen X, Huang X, Lu K. Science 2009;323:607.
[49] Arzt E. Acta Mater 1998;46:5611.
[50] Misra A, Hirth JP, Hoagland RG, Embury JD, Kung H. Acta Mater 2004;52:2387.
[51] Al-Fadhalah K, Tome CN, Beaudoin AJ, Robertson IM, Hirth JP, Misra A. Phil Mag 2005;85:1419.
[52] Anderson PM, Foecke T, Hazzledine PM. MRS Bull 1999;24:27.
[53] Misra A, Hirth JP, Kung H. Phil Mag A 2002;82:2935.
[54] Donohue A, Spaepen F, Hoagland RG, Misra A. Appl Phys Lett 2007;91:241905.
[55] Shan ZW, Stach EA, Wiezorek JMK, Knapp JA, Follstaedt DM, Mao SX. Science 2004;305:654.
[56] Schiotz J, Jacobsen KW. Science 2003;301:1357.
[57] Schiotz J, DiTolla FD, Jacobsen KW. Nature 1998;391:561.
[58] Hahn H, Mondal P, Padmanabhan KA. Nanostruct Mater 1997;9:603.
[59] Ivanisenko Y, Kurmanaeva L, Weissmueller J, Yang K, Markmann J, Rosner H, et al. Acta Mater 2009;57:3391.
[60] Zhu YT, Liao XZ. Nature Mater 2004;3:351.
[61] Kumar KS, Van Swygenhoven H, Suresh S. Acta Mater 2003;51:5743.
[62] Wu XL, Zhu YT, Wei YG, Wei Q. Phys Rev Lett 2009;103:205504.
[63] Li N, Wang J, Huang JY, Misra A, Zhang X. Scripta Mater 2010;63:363.
[64] Misra A, Verdier M, Lu YC, Kung H, Mitchell TE, Nastasi M, et al. Scripta Mater 1998;39:555.
[65] Hoagland RG, Kurtz RJ, Henager CH. Scripta Mater 2004;50:775.
[66] Wang J, Hoagland RG, Hirth JP, Misra A. Acta Mater 2008;56:5685.
[67] Rao SI, Hazzledine PM. Phil Mag A 2000;80:2011.
[68] Mitlin D, Misra A, Radmilovic V, Nastasi M, Hoagland R, Embury DJ, et al. Phil Mag 2004;84:719.
[69] Bellou A, Overman CT, Zbib HM, Bahra DF, Misra A. Scripta Mater 2011;64:641.
[70] Gruber PA, Böhm J, Onuseit F, Wanner A, Spolenak R, Arzt E. Acta Mater 2008;56:2318.
[71] Sinclair CW, Poole WJ, Bréchet Y. Scripta Mater 2006;55:739.
[72] Lu L, Schwaiger R, Shan ZW, Dao M, Lu K, Suresh S. Acta Mater 2005;53:2169.
[73] Ma E, Wang YM, Lu QH, Sui ML, Lu L, Lu K. Appl Phys Lett 2004;85:4932.
[74] Püschl W. Prog Mater Sci 2002;47:415.
[75] Bitzek E, Brandl C, Derlet PM, Van Swygenhoven H. Phys Rev Lett 2008;100:235501.
[76] Hoagland RG, Mitchell TE, Hirth JP, Kung H. Phil Mag A 2002;82:643.
[77] Embury JD, Hirth JP. Acta Metall Mater 1994;42:2051.
[78] Wang J, Hoagland RG, Hirth JP, Misra A. Acta Mater 2008;56:3109.
[79] Huang X, Hansen N, Tsuji N. Science 2006;312:249.
[80] Ungára T, Li L, Tichy G, Pantleon W, Choo H, Liaw PK. Scripta Mater 2011;64:876.
[81] Maaß R, Van Petegem S, Ma D, Zimmermann J, Grolimund D, Roters F, et al. Acta Mater 2009;57:5996.
[82] Koehler JS. Phys Rev B 1970;2:547.
[83] Li YP, Zhang GP. Acta Mater 2010;58:3877.
[84] Oh SH, Legros M, Kiener D, Dehm G. Nature Mater 2009;8:95.
[85] Dehm G. Prog Mater Sci 2009;54:664.
[86] Gruber PA, Solenthaler C, Arzt E, Spolenak R. Acta Mater 2008;56:1876.
[87] Kraft O, Gruber PA, Mönig R, Weygand D. Annu Rev Mater Res 2010;40:293.
[88] Fertig RS, Baker SP. Prog Mater Sci 2009;54:874.
[89] Zhang JY, Zhang X, Liu G, Wang RH, Zhang GJ, Sun J. Mater Sci Eng A 2011;528:7774.
[90] Kiener D, Grosinger W, Dehm G. Scripta Mater 2009;60:148.